# Simulation of a reacting gas–liquid bubbly flow with CFD and PBM: Validation with experiments☆

A. Buffo [a], M. Vanni [b], D.L. Marchisio [b],*

[a] Department of Biotechnology and Chemical Technology, School of Chemical Technology, Aalto University, Kemistintie 1 02150 Espoo, Finland
[b] Department of Applied Science and Technology, Institute of Chemical Engineering, Politecnico di Torino, C.so Duca degli Abruzzi 24, 10129 Torino, Italy

## ARTICLE INFO

## ABSTRACT

In this work we use computational fluid dynamics (CFD) to simulate a reactive gas–liquid bubbly system in a rectangular bubble column, operating at low superficial velocities (i.e. homogeneous regime). The gas bubbles, injected in the column through a sparger, contain one of the reactants, namely $CO_2$, that via mass transfer moves to the continuous liquid phase, where it reacts with NaOH. A key role is played by the bubble size distribution (BSD) and the specific surface area that define the overall mass transfer rate in the CFD model. In order to correctly predict the BSD and the polydispersity of the bubbly system the population balance equation is solved by the quadrature method of moments (QMOM), within the OpenFOAM (v. 2.2.x) two-fluid solver `compressibleTwoPhaseEulerFoam`. To reduce the computational time and increase stability, a second-order operator-splitting technique for the solution of the chemically reactive species is also implemented, allowing to solve the different processes involved with their own time-scale. To our knowledge this is the first time that QMOM is employed for the simulation of a real reactive bubbly system and predictions are validated against experiments.

© 2016 Elsevier Inc. All rights reserved.

## 1. Introduction

The simulation of reacting turbulent gas–liquid bubbly systems, via computational fluid dynamics (CFD), is complicated by the fact that the disperse phase, constituted by gas bubbles, is highly polydisperse, namely the gas bubbles are characterized by very different size values. Such polydispersity, observable even at low gassing rates in the so-called bubbly flow or homogeneous regime, can be even more pronounced when gas flow rates are larger, namely in the heterogenous regime. The fate of these bubbles, undergoing coalescence, breakage and mass transfer, is tightly coupled with the evolution of the continuous liquid phase, through the so-called phase-coupling [1,2]. A plethora of methods is available for the simulation of such systems and they are usually classified as: direct numerical simulations (DNS) [3], Euler–Lagrangian methods (ELM) [4,5] and Euler–Euler methods (EEM) [6–10]. This latter class of methods is the most suitable for the simulation of large pilot- and industrial-scale gas–liquid bubbly systems. EEM were originally formulated through a volume-average procedure,
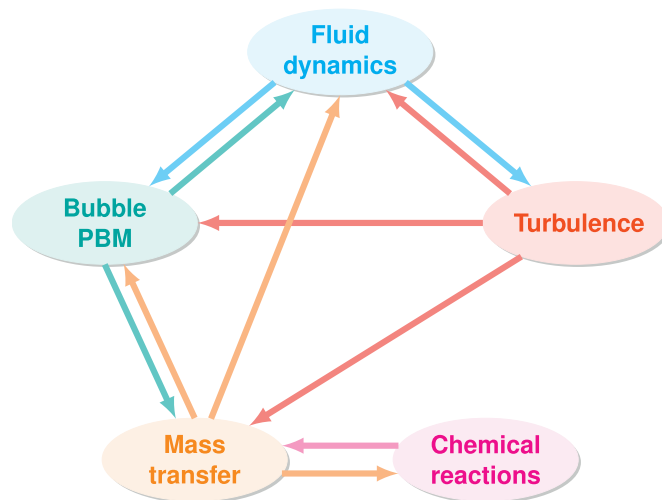
**Fig. 1.** Diagram showing the interdependency between different parts of the model.

but can also be derived by applying the moment method to the main governing equation of multiphase systems, namely the generalized population balance equation (GPBE), as explained by Marchisio and Fox [1].

In the latest years, a great effort has been put in the implementation and assessment of the coupling between different Population Balance Methods (PBM) with CFD codes for the description of polydisperse gas–liquid systems. Different methods can be divided into two large families: sectional-based [11–18], in which the bubble size distribution is divided into bins and the evolution of the number of the bubbles per each bin is acconted for, and moment-based [19–25], in which transport equations for some integral properties of the population of bubbles (i.e., moments of the bubble size distribution) are tracked. For an overview of different methods, readers may refer to specialized literature [1,26,27]

Moment-based methods have the advantage of making use of a smaller number of additional equations being suitable for the solution of large scale problems [28,29]. However, the moment transport equations are "unclosed" [30] and to overcome the closure problem the number density function is reconstructed by using a quadrature approximation [31–34]. The methods based on this approach are the so-called quadrature-based moment methods (QBMM) [1], that include the quadrature method of moments (QMOM), the direct quadrature method of moments (DQMOM) and the conditional quadrature method of moments (CQMOM). All of them have been implemented in different CFD codes for the simulation of gas–liquid systems. In particular QMOM has been used in Ansys Fluent for the simulation of stirred tanks [19] and in OpenFOAM for the simulation of bubble columns [35], DQMOM in TransAT for the simulation of gas–liquid pipe flows [36] and in Ansys Fluent for the simulation of stirred tanks [20], whereas CQMOM has been used in Ansys Fluent and OpenFOAM for the simulation of simultaneous bubble coalescence, breakage and mass transfer [37,38] as well as in an in-house code [39]. The performance of some of these methods has been compared [21] and recently reviewed [22].

To our knowledge however QBMM have never been used for the simulation of a reacting gas–liquid system, which is one of the test cases where they are most useful, as they are capable of predicting accurately the gas–liquid specific surface area, which in turn limits the mass transfer rate and eventually the chemical reaction rate. The application of this methodology to a similar problem gives the possibility to the model in a strongly coupled and complex manner to mimic the physical reality, as exemplified in Fig. 1. Following our previous work on this topic, our QMOM and CQMOM implementation in the OpenFOAM (v. 2.2.x) solver `compressibleTwoPhaseEulerFoam` [35] is used here to simulate a reacting gas–liquid system, for which experimental data are available in the literature [40]. It is important to stress here that the CFD model is fully predictive: all the model constants have been derived from theory and no fitting constants are adjusted here to match the experiments. The system investigated is very simple (Fig. 2): a rectangular bubble column is filled with a NaOH aqueous solution and $N_2$ is fluxed. Then abruptly the gas feed is changed to $CO_2$, which transfers to the liquid phase and reacts with NaOH. Eventually, experimental measurements concerning plume oscillation period, global gas hold-up, mean Sauter diameter of the bubbles, local gas velocity profile and pH time evolution are compared with model predictions.

## 2. Governing equations

As shown by Marchisio and Fox [1] by applying specific moment transforms to the GPBE the governing equations of fluid motion of phase $k$ are readily derived:

$$\frac{\partial \rho_k \alpha_k}{\partial t} + \nabla \cdot (\rho_k \alpha_k \mathbf{u}_k) = 0, \tag{1}$$
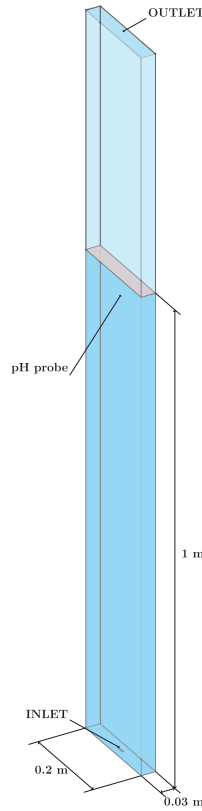
**Fig. 2.** Sketch of the bubble column investigated in this work.

$$\frac{\partial \rho_k \alpha_k \mathbf{u}_k}{\partial t} + \nabla \cdot (\rho_k \alpha_k \mathbf{u}_k \mathbf{u}_k) = -\nabla \cdot (\alpha_k \boldsymbol{\tau}_k) - \alpha_k \nabla p + \alpha_k \rho_k \mathbf{g} + \mathbf{F}_k, \tag{2}$$

where $k = l$ and $g$ for the continuous liquid phase and for the bubbly gaseous phase, respectively, and where $\alpha_k$ is the volume fraction, $\rho_k$ is the density and $\mathbf{u}_k$ is the Reynolds-averaged velocity for phase $k$. In the case of the liquid phase the stress tensor $\boldsymbol{\tau}_l$, following the Reynolds-averaged Navier–Stokes equation (RANS) approach, is expressed as:

$$\boldsymbol{\tau}_l = \mu_{\text{eff},l}\left((\nabla \mathbf{u}_l) + (\nabla \mathbf{u}_l)^T - \frac{2}{3}\mathbf{I}(\nabla \cdot \mathbf{u}_l)\right), \tag{3}$$

where $\mu_{\text{eff, l}}$ is the effective viscosity of the liquid phase: $\mu_{\text{eff,l}} = \mu_l + \mu_{t,l}$, and where in turn $\mu_l$ is the molecular viscosity of the liquid and $\mu_{t,l} = \rho_l C_\mu \frac{\kappa^2}{\epsilon}$, $\kappa$ is the turbulent kinetic energy of the liquid phase and $\epsilon$ is the energy dissipation rate of the liquid phase. Both are calculated from the corresponding transport equations:

$$\frac{\partial \alpha_l \kappa}{\partial t} + \nabla \cdot (\alpha_l \kappa \mathbf{u}_l) - \nabla \cdot \left(\alpha_l \frac{\mu_{t,l}}{\rho_l \sigma_\kappa} \nabla \kappa\right) = \alpha_l (G - \epsilon), \tag{4}$$

$$\frac{\partial \alpha_l \epsilon}{\partial t} + \nabla \cdot (\alpha_l \epsilon \mathbf{u}_l) - \nabla \cdot \left(\alpha_l \frac{\mu_{t,l}}{\rho_l \sigma_\epsilon} \nabla \epsilon\right) = \alpha_l \left(C_{\epsilon,1} \frac{\epsilon}{\kappa} G - C_{\epsilon,2} \frac{\epsilon^2}{\kappa}\right). \tag{5}$$

The model constants are those of the standard $\kappa - \epsilon$ model: $C_\mu = 0.09$, $\sigma_\kappa = 1.0$, $\sigma_\epsilon = 1.3$, $C_{\epsilon,1} = 1.44$, and $C_{\epsilon,2} = 1.92$. The term $G$ is the turbulence production rate defined as: $G = 2\frac{\mu_{t,l}}{\rho_l}(\mathbf{S}:\nabla \mathbf{u}_l)$, where the strain rate tensor is in turn defined as $\mathbf{S} = \frac{1}{2}(\nabla \mathbf{u}_l + (\nabla \mathbf{u}_l)^T)$.

The term $\mathbf{F}_k$ in Eq. (2) describes the interfacial forces (or momentum coupling) between the liquid and gas phase and is usually evaluated as the summation of drag, lift and virtual mass forces. Although the lift (and the virtual mass) force can be very important, especially for specific flow configurations [41,42], they are in this work neglected. This is justified by the fact that for the particular gas injection strategy used here, and for the rectangular shape of the bubble column, the role of these two forces is of secondary importance with respected to that of the drag force.

The drag model considered in this work is based on the following expression for the drag force coefficient [25]:

$$C_D = (1 - \alpha_g)^{C_A} \max\left[\frac{24}{Re_{\text{eff}}}\left(1 + 0.15 Re_{\text{eff}}^{0.687}\right), \frac{8}{3}\frac{Eo}{Eo + 4}\right], \tag{6}$$

where the Eotvos number is defined as: $Eo = (\rho_l - \rho_g)gd_{32}^2/\sigma$, whereas the effective Reynolds number is defined as follows:

$$Re_{\text{eff}} = \frac{\rho_l d_{32}|\mathbf{u}_l - \mathbf{u}_g|}{\mu^*} \quad \text{with } \mu^* = \mu_l + C_B\rho_l\frac{\kappa^2}{\epsilon}. \tag{7}$$

In the above equations $\rho_l$ and $\rho_g$ are the densities of the liquid and gas phases, $d_{32}$ is the mean Sauter diameter associated with the bubbles, $g$ is the gravity acceleration and $\sigma$ is the gas–liquid interfacial tension. In Eq. (6) two corrections are applied to the standard drag force coefficient expression. The first one is related to the so-called crowding or swarm effect. When bubbles are densely packed (i.e. $\alpha_g > 0.2$) their momentum boundary layers start interacting, resulting in non-linear effects on the drag force. The perceived drag force that each bubble "sees" is therefore higher that what predicted for a single isolated bubble [3,43], as witnessed by the larger gas hold-ups usually measured in "crowded" bubble columns, and as observed and quantified also in other multiphase systems [44]. The second correction is instead related to the so-called micro-scale turbulence, namely the turbulence on a length-scale smaller than the bubble size (that is therefore not resolved by the standard $\kappa - \epsilon$ model) as discussed in the literature [45], resulting again in an increase of the drag force coefficient [46]. Extensive comparison with experiments on different test cases working in the bubbly flow regime showed that a general good agreement can be obtained by using $C_A = -1.3$ and $C_B = 0.002$ [25]. These values were also used in this work.

As discussed by Marchisio and Fox [1] the polydispersity of the gas–liquid system can be written in terms of the bubble size distribution (BSD) and with QMOM the problem is treated by considering the moments of the BSD, defined as follows:

$$M_k(\mathbf{x}, t) = \int_0^{+\infty} n(L; \mathbf{x}, t)L^k dL, \tag{8}$$

where $k$ is in this case the moment order (usually ranging from 0 to $2N - 1$, where $N$ is the order of the quadrature approximation). Starting from the GPBE the following transport equation of the moment of order $k$ can therefore be obtained:

$$\frac{\partial M_k}{\partial t} + \nabla \cdot (\mathbf{u}_g M_k) = \overline{S}_k + \overline{G}_k, \tag{9}$$

where $\mathbf{u}_g$ is the Reynolds-averaged gas bubble velocity, $\overline{G}_k$ is the source term due to bubble growth/shrinking due to mass transfer and hydrostatic pressure variation, and where $\overline{S}_k$ is the source term due to coalescence and breakage, that with QMOM can be written as:

$$\overline{S}_k \approx \frac{1}{2}\sum_{\alpha=1}^N\sum_{\beta=1}^N w_\alpha w_\beta a_{\alpha,\beta}\left[\left(L_\alpha^3 + L_\beta^3\right)^{k/3} - L_\alpha^k - L_\beta^k\right] + \sum_{\alpha=1}^N w_\alpha f_\alpha\left(\overline{b}_\alpha^k - L_\alpha^k\right), \tag{10}$$

where $w_\alpha$ and $w_\beta$ are the $N$ weights and $L_\alpha$ and $L_\beta$ the $N$ nodes of the quadrature approximation of order $N$ built upon the first $2N$ moments of the BSD by using the Product-Difference algorithm [31,47,48]. $a_{\alpha,\beta} = a(L_\alpha, L_\beta)$ is the coalescence kernel and $f_\alpha = f(L_\alpha)$ is the breakage kernel both evaluated at the size nodes. The moment of order $k$ of the daughter distribution function is instead defined as:

$$\overline{b}_\alpha^k = \int_0^\infty L^k\beta(L|L_\alpha)dL. \tag{11}$$

Still with QMOM, the term $\overline{G}_k$ of Eq. (9) can be written as:

$$\overline{G}_k = k\sum_{\alpha=1}^N w_\alpha L_\alpha^{k-1}G_\alpha - \frac{k}{3}\frac{M_k}{\rho_g}\frac{D\rho_g}{Dt}, \tag{12}$$

where $G_\alpha = G(L_\alpha)$ is the rate of change of bubble size due to mass transfer evaluated at the size node $L_\alpha$ and the second right-hand side term accounts for the effect of the hydrostatic pressure on bubble size.

Several kernels have been proposed in the literature for breakage and coalescence [49,50]. Assuming that bubbles break up because of small turbulent eddies in the liquid bombarding the gas bubble surface, the following kernel can be used [51–53]:

$$f(L) = C_1\epsilon^{1/3}\text{erfc}\left(\sqrt{C_2\frac{\sigma}{\rho_l\epsilon^{2/3}L^{5/3}} + C_3\frac{\mu_l}{\sqrt{\rho_l\rho_g}\epsilon^{1/3}L^{4/3}}}\right), \tag{13}$$

where $\epsilon$ is the already introduced turbulent dissipation rate in the liquid. Although the kernel should have a very general validity and therefore should be valid for "any" gas–liquid system, some fine tuning of the three constants is always recommended. For air–water the following values have been suggested: $C_1 = 6.0$, $C_2 = 0.04$ and $C_3 = 0.01$.

As far as the daughter distribution function is concerned, a common choice is to use a $\beta-$Probability Density Function ($\beta$-PDF) [22], resulting in the following expression:

$$\overline{b}_k^\alpha = \frac{3240L_\alpha^k}{(k+9)(k+12)(k+15)}. \tag{14}$$

Different kernels have been proposed for coalescence and in the case of bubbles colliding due to turbulent fluctuations, one of the most popular is the following [22]:

$$a(L, L') = C_4 \epsilon^{1/3} \left(L + L'\right)^2 \left(L^{2/3} + L'^{2/3}\right)^{1/2} \exp\left(-C_5 \sqrt{\frac{2\rho_l \epsilon^{2/3}}{\sigma} \frac{LL'}{L + L'}}\right), \tag{15}$$

where in this work $C_4 = 0.88$ and $C_5 = 6 \times 10^9$. It is worth mentioning that the modeling parameters contained in both breakage and coalescence kernels are derived for air–pure water systems, however they might be different for other systems. Especially the parameter in the exponential part of Eq. (15), often referred as coalescence efficiency, can be very different as bubbles colliding in solution with electrolytes may repulse each other, diminishing the contact time needed for coalescence. However, kernels tackling this issue in a consistent way are not available, therefore the aforementioned kernels for air–water systems are used.

The rate of change of bubble size can be calculated through a simple mass balance for a single bubble:

$$G(L) = \sum_i \frac{2Ek_L M_{w,i}}{\rho_g} \left(\phi_{i,l} - H_i \phi_{i,g}\right), \tag{16}$$

where $k_L$ is the mass transfer coefficient, $E$ is the enhancement factor due to the chemical reaction, $M_{w,i}$ is the molecular weight, $\phi_{i,g}$ and $\phi_{i,l}$ are the concentrations in the gas and liquid phases, respectively, and where $H_i$ is the dimensionless Henry constant for the $i$-th species.

The CFD model is closed with additional transport equations related to the scalars involved in the chemical reactions. The typical transport equation for the $i$-th chemical component in the liquid phase reads as follows:

$$\frac{\partial \rho_l \alpha_l \phi_{i,l}}{\partial t} + \nabla \cdot (\rho_l \alpha_l \mathbf{u}_l \phi_{i,l}) - \nabla \cdot (\alpha_l \mathcal{D}_{i,\text{eff}} \nabla \phi_{i,l}) = -\rho_l k_L a \left(\phi_{i,l} - H_i \phi_{i,g}\right) + \rho_l S_{i,l}, \tag{17}$$

where $\mathcal{D}_{i,\text{eff}} = \mathcal{D}_i + \nu_t / Sc_t$, with $\mathcal{D}_i$ is the diffusion coefficient of the $i$-th species in the liquid, $\nu_t = \mu_{t,l}/\rho_l$ is the turbulent kinematic viscosity, $Sc_t$ is the turbulent Schmidt number (0.7 for liquids), $a = \pi M_2$ is the specific surface area of the gas bubbles and $S_{i,l}$ is the chemical source term. In this case, the only chemical species transferring from gas to liquid is $CO_2$, hence the transport equations for all the other chemical species considered only have the reactive term $\rho_l S_{i,l}$ as a source term of Eq. (17). The expressions used in this work to estimate the reaction kinetics and the enhancement factor $E$ are the same used in the work of Darmana et al. [40] and will be discussed in the next section.

The mass transfer coefficient, $k_L$, is generally calculated by using the penetration theory and by assuming that all the resistance is on the liquid side of the gas–liquid interface, resulting in the following expression [54]:

$$k_L = C_L \sqrt{\mathcal{D}_{CO_2} \sqrt{\frac{\epsilon}{\nu_l}}}, \tag{18}$$

where $C_L = 2/\sqrt{\pi}$. The chemical reactions are assumed to occur only in the liquid phase, as it will become clearer in the next section.
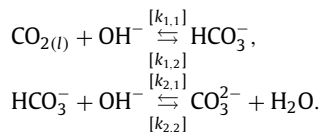
## 3. Experimental setup and numerical details

### 3.1. Experimetal setup and reaction kinetics

As previously mentioned, the experimental data for validate the model are taken from the work of Darmana et al. [40]. The bubble column experimentally investigated has a width of 200 mm, depth of 30 mm and height of 1500 mm. The front, back and both side walls are made of 10 mm thick glass plates, while the top and bottom part are made of stainless steel. During the experiment the column was filled with liquid up to a level of 1000 mm. Two types of experiments were carried out: firstly, a case without chemical reactions was investigated with nitrogen as gas phase and pure water as liquid phase. Then a reactive system was considered, with the continuous liquid phase as an aqueous solution of NaOH containing therefore hydroxyl ions, whereas the disperse gaseous phase as carbon dioxide. The following measurements were carried out during the experiments:

- Global gas holdup, by measuring the difference of liquid height in the column with and without bubbles.
- Time averaged bubble velocity profile, by using Particle Image Velocimetry (PIV) LaVision ImagePro 1200 HS camera equipped with a Nikkon 50 mm 1.8 AF lens. Measurements are carried out on a horizontal line in a middle cross section located 0.75 m above the inlet section of the column.
- Time evolution of pH, measured with a standard pH meter (Metrohm 691) during the reactive experiment.
- Local bubble size measurements, obtained through image analysis technique. Series of bubble images are recorded at different heights of the column with a CCD camera (Dalsa Motion Vision CA-D6-0512W). Data are available only for the reactive case.

While the non-reactive experiment was carried out by introducing the nitrogen in the column, with the measurements performed when the pseudo steady state typical of bubble columns was reached, the experiment involving chemical reactions were performed by employing the following protocol. The column is first filled with an aqueous solution containing hydroxyl ions, nitrogen is introduced until the flow pattern is fully developed and then the gas feed was abruptly switched to carbon dioxide. As a result of this change in the gas feed, the following reactions take place, while carbon dioxide is transferring from the gas to the liquid:

$$CO_{2(l)} + OH^- \underset{[k_{1,2}]}{\overset{[k_{1,1}]}{\rightleftarrows}} HCO_3^-,$$

$$HCO_3^- + OH^- \underset{[k_{2,2}]}{\overset{[k_{2,1}]}{\rightleftarrows}} CO_3^{2-} + H_2O.$$

This reacting system is therefore represented by five scalars: $\phi_{CO_2,g}$, $\phi_{CO_2,l}$, $\phi_{OH^-,l}$, $\phi_{HCO_3^-,l}$ and $\phi_{CO_3^{2-},l}$. The reaction kinetics of the forward first reaction (in m$^3$ kmol$^{-1}$ s$^{-1}$) is calculated through the following expression valid in the range of 291–314 K [40,55]:

$$\log\left(\frac{k_{1,1}}{k_{1,1}^\infty}\right) = 0.221I - 0.016I^2, \tag{19}$$

where $I$ is the ionic strength of the solution and $k_{1,1}^\infty$ is the reaction rate constant at infinite dilution and can be estimated as follows:

$$\log(k_{1,1}^\infty) = 11.895 - \frac{2382}{T}, \tag{20}$$

with the temperature $T$ expressed in K. The backward rate constant of the first reaction, $k_{1,2}$ (s$^{-1}$), can be determined by considering the equilibrium constants, $K_3$ and $K_w$, of the two following reactions:

$$CO_{2(l)} + H_2O \rightleftarrows HCO_3^- + H^+$$

$$H^+ + OH^- \rightleftarrows H_2O$$
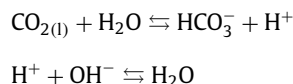
where the equilibrium constant of the first reaction, $K_3$ (kmol m$^3$), can be evaluated by means of the following equation [40,56]:

$$K_3 = \frac{\phi_{HCO_3^-,l}\phi_{H^+,l}}{\phi_{CO_2,l}} = \exp\left(-\frac{12092.1}{T} - 36.786\log(T) + 235.482\right), \tag{21}$$

and the equilibrium constant of the second reaction, $K_w$ (kmol$^2$ m$^{-6}$), can be calculated as [40,57]:

$$K_w = \phi_{H^+,l}\phi_{OH^-,l} = 10^{-5839.5/T+22.4773\log_{10}(T)-61.2062}. \tag{22}$$

The backward reaction kinetics $k_{1,2}$ is then calculated considering that:

$$K_1 = \frac{k_{1,1}}{k_{1,2}} = \frac{K_3}{K_w}. \tag{23}$$

The second reaction is an extremely fast proton transfer and its forward rate constant, $k_{2,1}$, is of the order of $10^{10}$–$10^{11}$ m$^3$ kmol$^{-1}$ s$^{-1}$ [40,58]. The backward reaction rate $k_{2,2}$ (s$^{-1}$) can be estimated through the equilibrium constant $K_2$ (m$^3$ kmol$^{-1}$) [40,59]:

$$K_2 = \frac{k_{2,1}}{k_{2,2}}, \tag{24}$$

with

$$\log\left(\frac{K_2}{K_2^\infty}\right) = \frac{1.01\sqrt{\phi_{Na^+,l}}}{1 + 1.27\sqrt{\phi_{Na^+,l}}} + 0.125\phi_{Na^+,l}, \tag{25}$$

$$\log(K_2^\infty) = \frac{1568.94}{T} + 0.4134 - 0.00673T. \tag{26}$$

It is worth mentioning that in the work of Darmana et al. [40] a value of $k_{2,1} = 10^6$ m$^3$ kmol$^{-1}$ s$^{-1}$ was used in the numerical simulations due to stability issues, while here a value of $k_{2,1} = 10^{10}$ m$^3$ kmol$^{-1}$ s$^{-1}$ was used due to the numerical stability guaranteed by the operator splitting approach.

A summary of the physical constants employed in the simulations is reported in Table 1. The Henry constant $H$ for the CO$_2$ in aqueous electrolytic solution can be calculated by means of the method of Weisenberger and Schumpe [60], for solutions in a range between 293 and 303 K:

$$\log\left(\frac{H_w}{H}\right) = \sum(h_i + h_g)\phi_{i,l}, \tag{27}$$

**Table 1**
Physical properties used in the numerical simulations.

| | | |
|---|---|---|
| $\rho_l$ | 998.2 | kg m$^{-3}$ |
| $\rho_g$ | 1.842 | kg m$^{-3}$ |
| $\mu_l$ | $1.0 \times 10^{-3}$ | Pa s$^{-1}$ |
| $\sigma$ | 0.07 | N m$^{-1}$ |

**Table 2**
Parameters for the calculation of the Henry constant $H$, Eq. (27) [60].

| Ion | $h_i$ (m$^3$ kmol$^{-1}$) | Gas | $h_g$ (m$^3$ kmol$^{-1}$) |
|---|---|---|---|
| Na$^+$ | 0.1171 | CO$_2$ | $-0.0183$ |
| OH$^-$ | 0.754 | | |
| HCO$_3^-$ | 0.1372 | | |
| CO$_3^{2-}$ | 0.1666 | | |

where the parameters $h_i$ and $h_g$ are reported in Table 2, and the Henry constant for $CO_2$ in pure water, $H_w$, can be calculated as [40,61]:

$$H_w = 3.59 \cdot 10^{-7} RT \exp\left(\frac{2044}{T}\right). \tag{28}$$

The diffusivity of $CO_2$ into aqueous electrolyte solutions, $\mathcal{D}_{CO_2}$, can be estimated by using the model of Ratcliff and Holdcroft [62]:

$$\frac{\mathcal{D}_{CO_2}}{\mathcal{D}_{w,CO_2}} = 1 - 1.29 \cdot 10^{-4} \phi_{OH^-,l}, \tag{29}$$

where the diffusion of $CO_2$ in pure water, $\mathcal{D}_{w,CO_2}$, is calculated by means of the following relationship [40,61]:

$$\mathcal{D}_{w,CO_2} = 2.35 \cdot 10^{-6} \exp\left(-\frac{2119}{T}\right) \quad (\text{m}^2\text{s}^{-1}). \tag{30}$$

The enhancement factor $E$ is estimated by using the expression given by Westerterp et al. [40,63]:

$$E = \begin{cases} -\frac{Ha^2}{2(E_\infty-1)} + \sqrt{\frac{Ha^4}{4(E_\infty-1)^2} + E_\infty\frac{Ha^2}{E_\infty-1} + 1} & E_\infty > 1 \\ 1 & E_\infty \leq 1, \end{cases} \tag{31}$$

where

$$E_\infty = \left(1 + \frac{\mathcal{D}_{OH^-}\phi_{OH^-,l}}{2\mathcal{D}_{CO_2}H\phi_{CO_2,g}}\right)\sqrt{\frac{\mathcal{D}_{CO_2}}{\mathcal{D}_{OH^-}}}, \tag{32}$$

$$Ha = \frac{\sqrt{k_{1,1}\mathcal{D}_{CO_2}\phi_{OH^-,l}}}{k_L}. \tag{33}$$

This approximate formula is faster than a rigorous calculation for the enhancement factor and it has an accuracy within 10% [40].

### 3.2. Numerical details

As clearly depicted in Fig. 1, the whole model is constituted by different interdependent parts, having each one its own time scale. As pointed out by Darmana et al. [40], the reaction kinetics are vary fast compared to the time scales of bubble coalescence, breakage and mass transfer, and, more in general, of fluid dynamics. This means that if a coupled approach is used to solve the governing equations, a high-order time integrator combined with a very small time step is advisable to reduce the error associated with the time integration. In a preliminary analysis we investigated the influence of the time step on the results in case of a coupled approach and first-order backward Euler scheme as time integrator, showing that a $\Delta t \approx 10^{-5}$ s was needed to have a time step-independent solution without any issue in terms of numerical stability. This value is about two order of magnitude lower than the one usually adopted for the solution of bubble dynamics in bubble columns working under similar operating conditions [25,35,64], significantly increasing the computational time needed. It is also worth mentioning that the usage of larger time steps in this case leaded to numerical issues that undermine the stability of the simulation. In addition, in practical CFD computations high-order time integrator are rarely used only in a few specific applications (such as detailed turbulence simulation with LES or DNS, reactive systems with fast kinetics) [65], therefore the implementation of time integration schemes of order higher than second is usually not available in existing CFD codes.
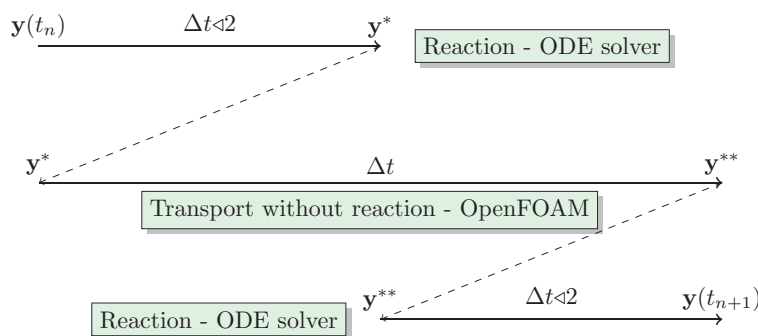
**Fig. 3.** Schematic representation of the operator-splitting approach.

A way to speed up the solution of similar problems is offered by the operator splitting approach. With this solution technique it is possible to decouple the fast reaction kinetics from the fluid dynamics, integrating in time the different terms of a transport equation, each one with the proper numerical scheme [66–68]. In this way, the transport equations for all the quantities can be solved through standard time integrators, while chemical species transport equations are solved using the operator splitting approach, allowing us to run simulations in a feasible time. However, this procedure has also drawbacks since introduces an additional time integration error, often referred as splitting error, whose magnitude depends on the time step and on the order of accuracy of the procedure. Therefore, in this work we adopted the so-called Strang operator splitting approach [67], which is a second-order accurate. This method based on idea of dividing the single time step in two equal parts. The chemical reaction source term is then applied for half of the time step, by updating the local concentration values. Subsequently physical transport is applied, by updating the chemical species concentration for an entire time step, and finally the chemical reaction term is applied for the remaining half time step. A schematic representation of the algorithm is reported in Fig. 3. In this way, a high-order time integration procedure is retained, while the simulation stability is increased and the computational costs reduced, since a larger time step, corresponding to the one needed to solve the fluid dynamics details, can be used. In the present case, the reaction source term are solved by means of a high-order ODE integrator specific for stiff problems (the backward differentiation formula method implemented in the library LSODE, [69]), while the other terms of the chemical species transport equations (and all the other governing equations) are solved with the standard second-order backward Euler scheme, with a fixed time step equal to $2 \times 10^{-3}$ s.

As previously mentioned, the numerical simulations were carried out with OpenFOAM (v. 2.2.x) two-fluid solver `compressibleTwoPhaseEulerFoam`, since the open source framework gives us the freedom to hard-code every single aspect of the numerical procedure. For example, the moment transport equations are implemented by using a specific approach that intrinsically preserves the properties of moment boundedness and realizability [64]. In addition, the operator splitting approach was easily integrated into the solver structure without any particular artifice, often required when commercial codes are employed for implementing new features.

The final mesh employed in the simulations was constituted by $62 \times 19 \times 128$ cells in the three directions. The gas spager was modeled as a gas velocity inlet boundary condition, assuming an instantaneous equilibrium between liquid and gas, while at the top of the column outflow boundary condition was used. All the other surfaces were described as walls (with no-slip condition). As far as the inlet boundary conditions for the $CO_2$ bubbles are concerned, we assumed a lognormal bubble size distribution with mean estimated through the correlation of Geary and Rice [70] and standard deviation equal to 15% of the mean value, as suggested by Laakkonen et al. [52] for holed sparger. This correlation predicts a mean bubble diameter of 6.2 mm, which is higher than the value used by Darmana and coworkers in their simulation [40] (i.e., 5.5 mm) and likely coming from experimental evidences. The reader may refer to our previous work [35] for further details on the bubble inlet condition.

To investigate what is the influence of the different parts of the model, different simulations are carried out. Firstly, the case without chemical reaction, for which experimental data of global gas hold-up and a time-averaged gas velocity profile at one height of the column are available, is simulated. Then, the chemical reaction experiment is simulated by assuming three different fixed and constant bubble sizes (3, 5 and 7 mm, respectively), to highlight the effect of a similar choice on the interfacial area and, indirectly, on mass transfer rates, chemical reactions and fluid dynamics. Eventually, the full model with bubble sizes predicted with the population balance and chemical reactions is solved and the results are compared with the experimental data available. Moreover, another inlet condition (i.e., mean inlet bubble diameter of 5.5 mm) was considered to see the influence of this aspect on the final results.

The simulation of the chemical reaction experiment completely mimics the experimental protocol described above: preliminary an inert gas (nitrogen) is fluxed into the column filled with a NaOH solution with an initial pH of 12.5, in order to have a fully developed flow field as in the experiment. After this initial time interval (equal to 30 s in our simulations, which is three times larger than needed as the flow field is fully developed after about 10 s), pure $CO_2$ is fed through the gas sparger at a gas flow rate of 46.2 ml/s (i.e. 2.2 ml/s at each one of the 21 injection needles) and the calculation of
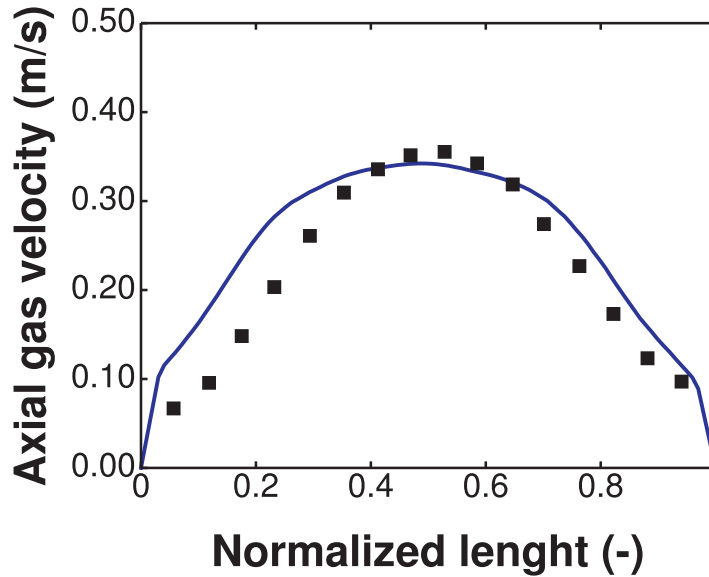
**Fig. 4.** Comparison between experiment (black squares) and simulation (blue solid line) in terms of the time-averaged axial gas velocity profile for the case without chemical reactions. Measurements are carried out on a horizontal line located at the center of the column at height equal to 0.75 m. (For interpretation of the references to color in this figure legend, the reader is referred to the web version of this article).

**Table 3**
Comparison of experimental data and predictions in terms of global gas hold-up and plume oscillation period (POP) for all the test cases investigated: PBM refers to the full model with mean inlet bubble size calculated with Geary and Rice correlation [70], CF1 to the case without PBM with constant and fixed bubble size equal to 3 mm, CF2 to the case with constant and fixed bubble size equal to 5 mm, CF3 to the case with constant and fixed bubble size equal to 5 mm and PBM2 to the full model with mean inlet bubble size equal to 5.5 mm as in the work of Darmana et al. [40].

|                | No reactions | | Reactive case | | | | | |
|----------------|------|------|------|------|------|------|------|------|
|                | Exp. | Sim. | Exp. | PBM  | CF1  | CF2  | CF3  | PBM2 |
| Gas hold-up (%) | 2.3  | 1.8  | 1.3  | 1.0  | 0.8  | 1.1  | 1.4  | 1.1  |
| POP (s)         | 5.8  | 6.7  | 10.2 | 9.1  | 10.6 | 9.4  | 9.2  | 9.6  |

the reaction kinetics is activated: through the mass transfer mechanism, some of the $CO_2$ contained in the gas bubbles will move to the liquid with the consequent start of the reversible two-step reactions reported above.

## 4. Results and discussion

### 4.1. Experiment without chemical reactions

Let us start the discussion of the results by presenting first the case without chemical reaction. Fig. 4 and Table 3 report the comparison between numerical predictions and available experimental data, namely the time-averaged gas velocity profile at one horizontal line located at the center of the column at height equal to 0.75 m, the global gas hold-up and the plume oscillating period. It is worth reminding that the non-reactive system is constituted of a nitrogen–pure water system and there is no mass exchange between gas and liquid phases: this system is very close to the standard air–pure water system for which the sub-models for describing the bubble coalescence, breakage and momentum exchange with the continuous phase are formulated. The general good agreement obtained for this case shows that the adopted sub-models are adequate for predicting the mean flow characteristics of the investigated system. A similar result is in line with our previous validation work [25], where different pieces of gas–liquid equipment operating in the bubbly flow regime as in this case were studied. Moreover, it is also important to remark the fact that in a CFD-PBM the bubble size is not a parameter of the simulation, but it is calculated through the PBM: although for this case there are no measurements of bubble size, the good agreement obtained for the fluid dynamic quantities is an indirect confirmation of the model capability of capturing the physical reality.
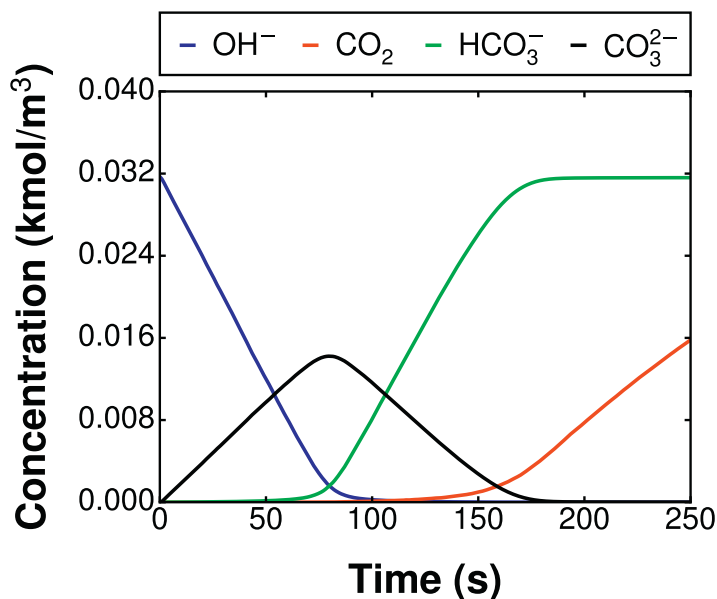
**Fig. 5.** Time evolution of the volume-averaged chemical species concentrations involved in the reaction resulting from the numerical simulation.

## 4.2. Chemical reaction experiment

### 4.2.1. Reaction progression and fluid dynamics quantities

All the simulation results reported in this section refer to the full CFD-PBM simulation, with inlet mean bubble size calculated with the correlation of Geary and Rice [70]. As previously mentioned, when carbon dioxide is fed in the column containing the NaOH solution, the reversible two-step reactions producing bicarbonate ($HCO_3^-$) and carbonate ($CO_3^{2-}$) occur. Fig. 5 reports a typical example of the species concentration time evolution predicted by the kinetic model: as shown in the first 80 s the second reaction prevails over the first and the production of carbonate ions reaches its maximum. However, with the progressive consumption of hydroxyl ions and the mass transfer of carbon dioxide from gas to liquid, after the first 80 s the equilibrium of the second reaction shifts to left and the bicarbonate ions starts to accumulate in the system. The picture at 250 s, which is close to the final equilibrium, is clear: the concentration of bicarbonate ions is not increasing anymore, mainly because hydroxyl ions were completely consumed by the reactions, while dissolved $CO_2$ which is no more involved in the production of bicarbonate is accumulated in the system. The concentration solubility of carbon dioxide is not reached after 250 s, but the system can be considered as non-reactive after this time.

Fig. 6 show instantaneous contour plots at different time steps of the chemical species involved during the reactive process. As it is possible to observe, at $t = 10$ s all the dissolved $CO_2$ immediately reacts with hydroxide ions ($OH^-$) in the beginning of the process and it is directly converted into carbonate ($CO_3^{2-}$). This means that in this phase the bicarbonate ion ($HCO_3^-$) concentration is almost equal to zero in all the domain. Then, approximately after 80 s from the start of the reaction, the carbonate concentration reaches a maximum and then decreases; simultaneously, the bicarbonate concentration starts to increase. This situation can be observed also in Fig. 6 (second row). After about 200 s from the beginning of the reaction experiment, the concentration of the bicarbonate ions reaches the initial concentration, while it goes to zero almost everywhere in the reactor. At this point, the chemical reaction rates diminish and the dissolved carbon dioxide starts to accumulate in the liquid in the entire column, as it is possible to see in Fig. 6 (third row).

It is also interesting to point out the behavior of hydrodynamics quantities during the reaction. In Fig. 7 the time evolution of the global gas hold-up is reported. As can be observed, the global gas hold-up is a dynamic variable during the reaction. In fact, the global gas hold-up first decreases and stays constant during the reaction stage dominated by the transfer of $CO_2$ into the liquid phase, then it starts increasing approximately when the bicarbonate ion saturated the liquid phase. Fig. 8 shows the instantaneous contour plots of the gas volume fraction at three different times. As it is possible to see, the flow field has a typical shape of partially aerated columns, with the central bubble plume oscillating from side to side: this reflects the transient and instantaneous behavior of liquid flow macrovortices that characterize the column flow fields.

Fig. 9 reports the instantaneous contour plot of the local values of mean Sauter diameter at three different times. It is important to remark that this is the main outcome of a CFD-PBM model, where the bubble size is not used as a fitting parameter, but is instead calculated through the solution of the GPBE, after proper definition of bubble coalescence and breakage rates. As previously mentioned, in a reactive case as the one we are investigating the knowledge of the bubble size distribution is ever more important, as the mass transfer rates significantly depend on the bubble interfacial area. Fig. 9 shows the value of the $d_{32}$ only in the regions where the local gas volume fraction is higher than $1 \times 10^{-5}$, as the
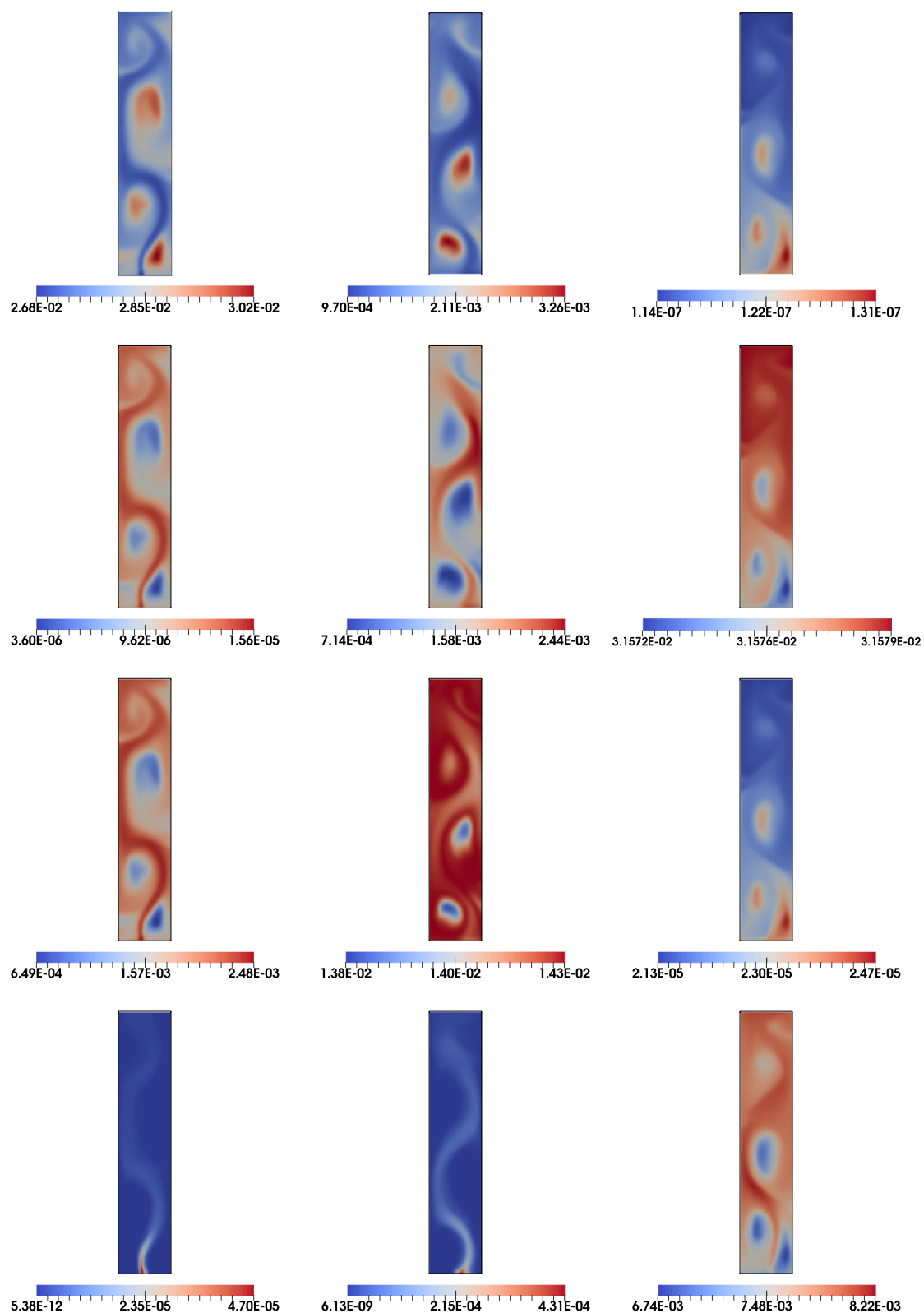
**Fig. 6.** Instantaneous contour plots of the chemical species involved in the reaction. From top to bottom: $OH^-$, $CO_3^{2-}$, $HCO_3^-$, dissolved $CO_2$ (Concentrations in $kmol/m^3$), From to left to right: time equal to 10 s, 80 s and 200 s.
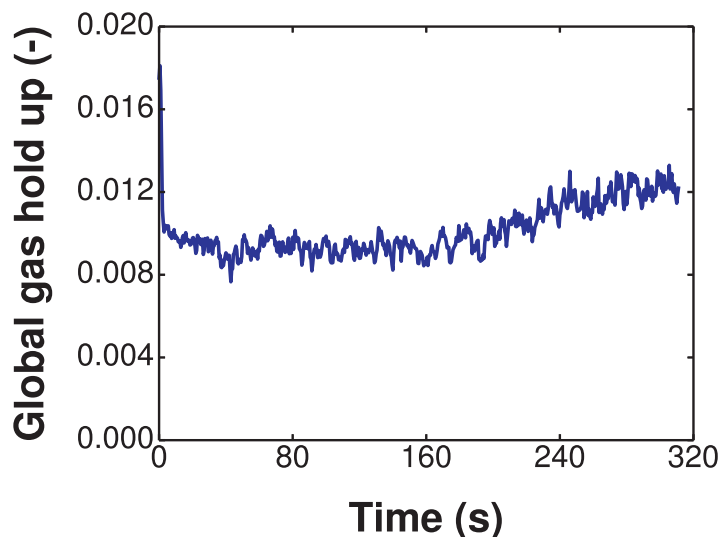
**Fig. 7.** Time evolution of the global gas hold-up predicted by the model during the reactions.
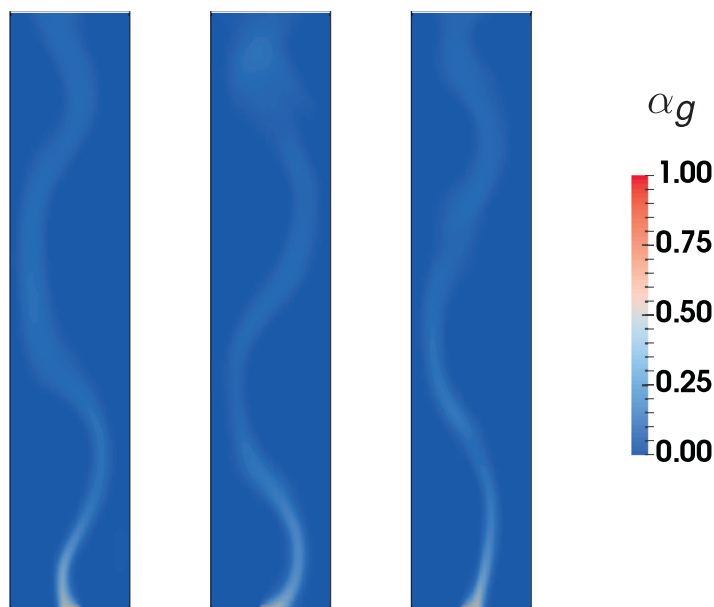


**Fig. 8.** Instantaneous contour plots of the gas volume fraction at three different times. From left to right: 10 s, 80 s and 200 s.

values given by the model in the regions where the gas volume fraction is lower are not meaningful due to the almost absence of bubbles in those areas. As can be seen from the figure, the bubbles are larger in the bottom region of the column near the sparger, where most of the coalescence takes place, while are smaller in the upper part which is instead dominated by the bubble breakage. These were only a few examples of the detailed information that the model is able to give, pointing out the need of a validation through comparison with experiments to assess the its capability to reproduce the physical reality.

### 4.2.2. Validation with experimental data

For the validation of such a complex model, it is always advisable to have instantaneous/time-averaged measurements for both local and global quantities. However, apart from technical limitations, similar experimental campaigns can be very expensive. Therefore, in most of the cases the available experimental data are scarce, limiting the possibility to improve the modeling effort. In this case, numerous experimental data are available and the comparison with the simulation results is reported in this section. For the moment, let us limit the discussion only on the results obtained with the full CFD-PBM model with inlet mean bubble size calculated with the correlation of Geary and Rice [70], as we consider this as our
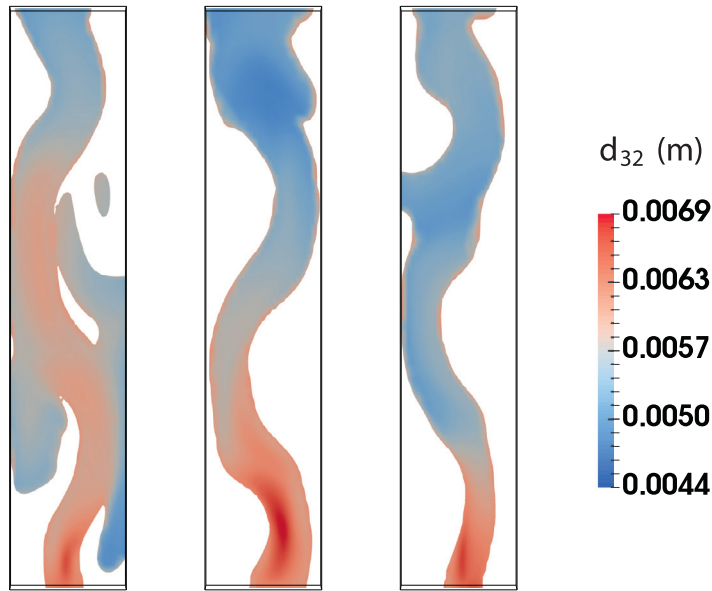
**Fig. 9.** Instantaneous contour plots of the mean Sauter diameter (in m) at three different times. Only zones with $\alpha_g > 1 \times 10^{-5}$ are drawn. From left to right: 10 s, 80 s and 200 s.
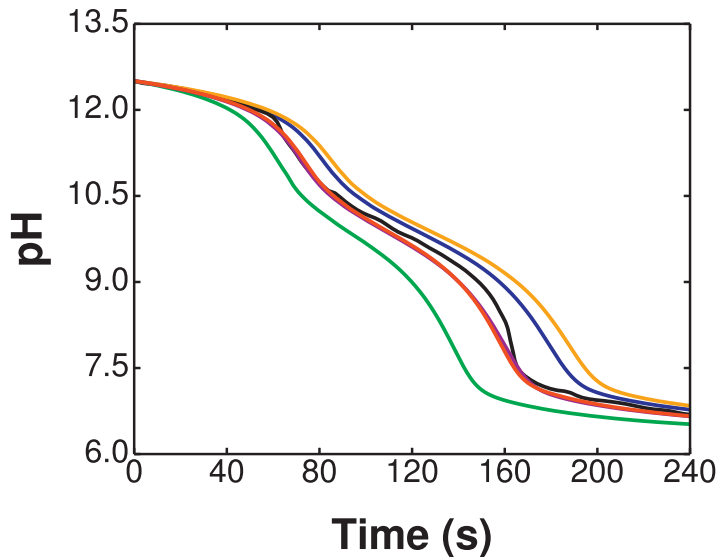


**Fig. 10.** Comparison between predicted and experimental pH evolution in one point of the domain, located at $x = 0.1$ m, $y = 0.15$ m and $z = 0.95$ m. Black line: experimental data. Blue line: CFD-PBM prediction with mean inlet bubble diameter calculated with Geary and Rice correlation [70]. Green line: prediction with constant and fixed bubble size equal to 3 mm. Purple line: prediction with constant and fixed bubble size equal to 5 mm. Orange line: prediction with constant and fixed bubble size equal to 7 mm. Red line: CFD-PBM prediction with mean inlet diameter equal to 5.5 mm as in the work of Darmana et al. [40]. Purple and red line are partially overlapping. (For interpretation of the references to color in this figure legend, the reader is referred to the web version of this article).

"standard" settings since it was proven to give good agreement with the experiments on many other test cases [25]. Fig. 10 shows the experimental time evolution of pH in one point of the domain compared with the numerical prediction. This comparison give us not only an important information about the time evolution of one chemical component (hydroxyl ions) but also an indirect knowledge of mass transfer rates and all the other chemical species involved in the reaction. The slope of the first part of the curve is determined by the mass transfer rates, as $OH^-$ ions rapidly react with dissolved $CO_2$, then after 80 s we observe a change in the curve slope, which is caused by the shift of equilibrium of the second reaction (around pH 11) in favor of bicarbonate. Another change in pH slope is observed at about 200 s, when the first reaction is shifted towards dissolved carbon dioxide, at pH approximately of 7.5. Through the comparison between experiment and simulation shown in Fig. 10 it is possible to conclude that the model is able to properly predict the time evolution of the reactions. From the qualitative point of view, the predicted pH curve shows a similar trend, with the change in the slope as observed
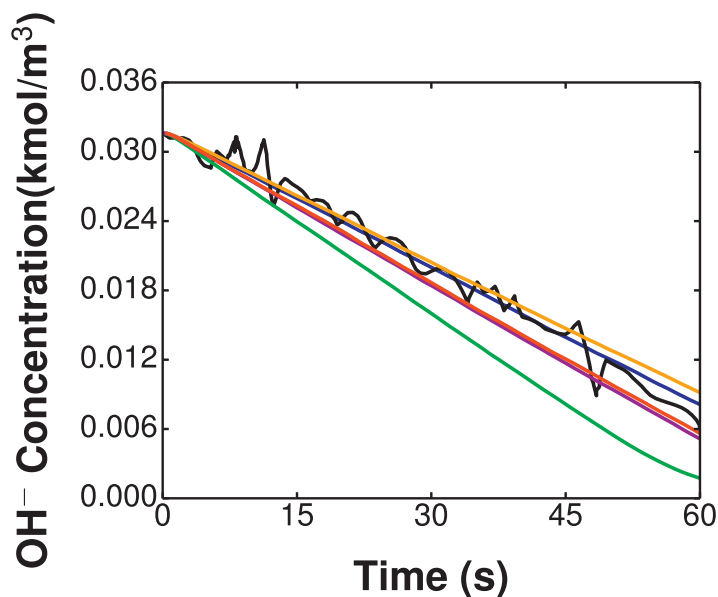
**Fig. 11.** Comparison between predicted and experimental time evolution of $OH^-$ concentration (kmol m$^{-3}$) during the first 60 s of the reaction in one point of the domain, located at $x = 0.1$ m, $y = 0.15$ m and $z = 0.95$ m. The color scheme is the same as in Fig. 10. (For interpretation of the references to color in this figure legend, the reader is referred to the web version of this article).

in the experiment. From the quantitative point of view instead, it is possible to notice that the two curves are overlapped in the first 60 s, as also the comparison between simulation and experiment for the $OH^-$ concentration reported in Fig. 11 shows. However, after 60 s the predicted pH evolution is slightly lagging behind compared to the experimental one; possible reasons of such disagreement can be the description of the second reaction, which is modeled with a finite-rate reaction through a high kinetic constant, instead of being considered instantaneous. Another reason could be the prediction of the bubble size distribution as we will see in the following section.

Table 3 shows further comparison with the experimental data, in terms of some fluid dynamics quantities such as global gas hold-up and plume oscillating period (POP). The global gas hold-up is calculated by first volume-averaging, in the region occupied by the liquid, the gas volume fraction and then time-averaging after a preliminary transient time in case of non-reacting simulation or time-averaging from 20 s to 95 s (corresponding to the time interval in which the global gas holdup is approximately constant, as shown in Fig. 7). The POP is instead calculated by operating the Fourier transform of the pressure signal in one point of the geometry. As it is possible to notice, there is good agreement for such quantities, showing how this methodology is capable of properly predicting the fluid dynamic behavior of bubble columns in the homogeneous regime.

Fig. 12 reports the comparison between experiment and prediction in terms of the time-averaged gas velocity profile, carried out at one horizontal line located in the center of the column at height equal to 0.75 m. The time-averaging procedure is also in this case performed for the time interval from 20 s to 95 s. As it is possible to observe by comparing Fig. 4 with Fig. 12, the experimental profile is very similar to the case without chemical reactions, but the local values are lower than the case without reactions. Also the simulation seems to capture this behavior, as the values predicted in the chemical reaction case is lower than in the non-reactive case. However, the simulation here seems to slightly overpredict the gas velocity profile: even though the comparison can be considered satisfactory due to the experimental uncertainties, such difference might be due to the phase coupling (e.g., drag coefficient) or turbulence models that are just approximations of the physical reality. Moreover, this might be the cause of the slight underprediction of the global gas holdup shown in Table 3, as bubbles moving faster have lower residence time in the column.

Another aspect influencing the fluid dynamics predictions is also the bubble size distribution. Fig. 13 shows the comparison between simulation and experiment for the time-averaged local mean Sauter diameter, measured at different heights of the column. The $d_{32}$ from the simulation is calculated by the time-average values from different points belonging to a line that connects two points: the central point at the top and at bottom of the column. The experimental values, instead, are likely estimated through volume-averaging procedure of the bubbles identified in each single snapshot taken by the CCD camera. Due to the experimental uncertainties, this comparison should be considered qualitative rather than qualitative, as explained in the original work of Darmana et al. [40]. As it is clear from the picture, the experimental trend is reproduced by the simulation, with the mean bubble diameter decreasing with the distance from the gas distributor because of the consumption of the carbon dioxide. This behavior might be caused by the bubble breakage and shrinking due to mass transfer prevailing over bubble coalescence and expansion due to hydrostatic pressure changes. However, the present model seems to over-predict the bubble size: this is in contradiction with other comparisons shown before, as the one for the $OH^-$ con-
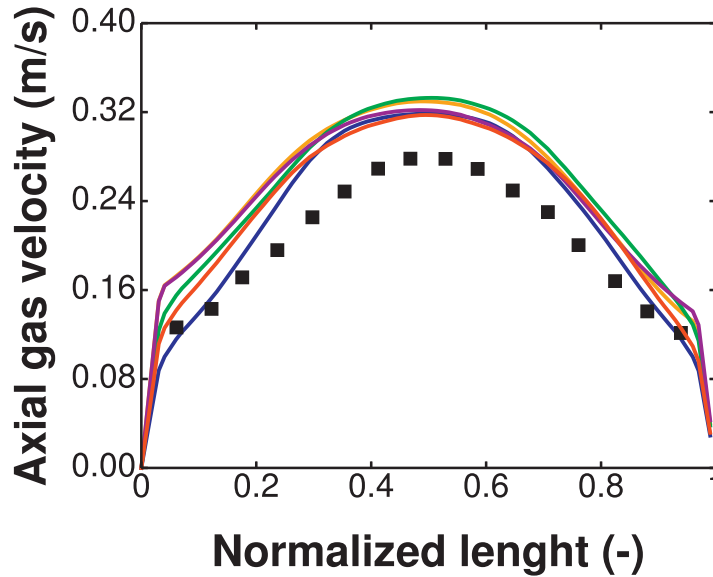
**Fig. 12.** Time-averaged axial gas velocity profile for the case with chemical reactions. Measurements are carried out on a horizontal line located at the center of the column at height equal to 0.75 m. The color scheme is the same as in Fig. 10. (For interpretation of the references to color in this figure legend, the reader is referred to the web version of this article).
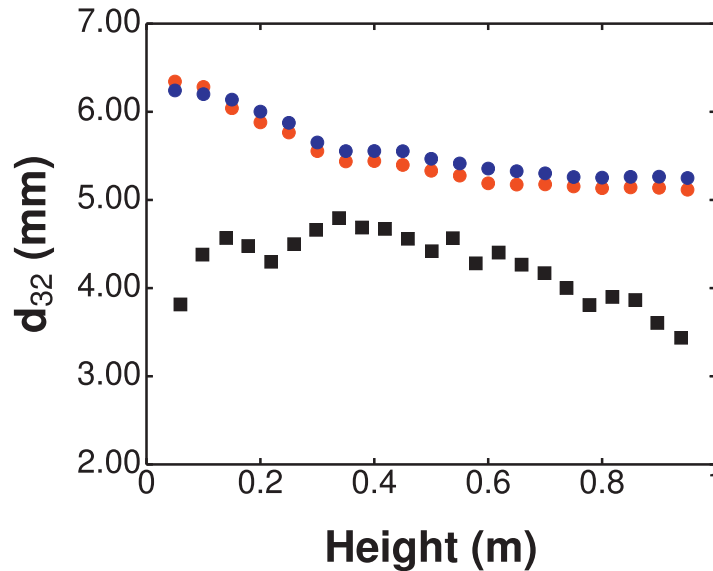


**Fig. 13.** Comparison between prediction and experimental measurement for the time-averaged mean Sauter diameter $d_{32}$ (mm) at different heights of the column. Black squares: experimental data. Blue circles: CFD-PBM prediction with mean inlet bubble diameter calculated with Geary and Rice correlation [70]. Red circles: CFD-PBM prediction with mean inlet diameter equal to 5.5 mm as in the work of Darmana et al. [40]. (For interpretation of the references to color in this figure legend, the reader is referred to the web version of this article).

centration in the early stages of the reaction, which proves that the mass transfer rate of $CO_2$ is properly predicted by the model. It is worth mentioning that the bubble diameter varies not only from point to point in the column, but also with time during the reaction: a precise information about the time interval at which the visual bubble diameter measurements have been performed is not reported in the experimental work. Here we considered the same time interval adopted for the calculation of the global gas holdup to carry out the time-averaging procedure. In addition, also the exact position of the camera is not known, as well as the total number of bubbles per measurement point: this information is crucial for a detailed validation. In the absence of these, we can conclude that also this comparison is satisfactory. However, due to this difference between predicted and experimental mean Sauter diameter, it is interesting to investigate the influence of the bubble size on the mass transfer rates and fluid dynamics quantities. This is done by performing simulations with different fixed and constant bubble size (i.e., without population balance) and with different initial conditions.

### 4.2.3. Effect of bubble size: fixed size and different inlet condition

Now let us focus on the results obtained in the other simulations carried out, such as with different constant and fixed bubble sizes and different mean inlet bubble diameter. As previously mentioned, the effect of different fixed and constant bubble sizes was investigated: such approach can be considered as a less sophisticated approach to treat bubble polydispersity. In fact, the bubble size is not predicted through a model but becomes a pure fitting parameter of the simulation, as it needs to be guessed to obtain the best agreement with the experiments. Moreover all the bubbles are implicitly assumed to have the same size, in contrast with what is done with QMOM. Figs. 10–12 and Table 3 reports, respectively the comparison with the experiment in terms of pH time evolution, time evolution of OH$^-$ concentration, time-averaged gas velocity profile, global gas hold-up and plume oscillating period. As can be seen from Fig. 10 and Fig. 11, mass transfer rates are significantly influenced by the bubble size as expected, with the smallest diameter giving the highest interfacial area and therefore the fastest mass transfer rates, even faster than the actual decay of pH observed experimentally. The best agreement seems to be obtained with bubble size equal to 5 mm, which is a size close the range predicted by the CFD-PBM simulations, as it is shown in Fig. 13. The comparison in terms of the time-averaged axial gas velocity profile reported in Fig. 12 shows that there is no a clear trend, mainly because the drag experienced by the bubbles in the investigated size range is approximately the same as they all reach the same bubble terminal velocity at the equilibrium [71]. If we look at the prediction of global quantities instead, such as the global gas holdup and the plume oscillating period reported in Table 3, a clear trend can be observed: with the increase of the bubble size, the gas hold-up increases and the plume oscillating period decreases, with the constant and fixed size of 5 mm giving the best agreement with the experiment.

The last test case here studied involved a different inlet condition for the bubble population, i.e., assuming a log-normal distribution with mean bubble size equal to 5.5 and standard deviation equal to 15% of the mean diameter. As mentioned earlier, this latter initial condition is closer to the condition imposed by Darmana et al. [40] in their simulation, likely coming from experimental evidences, as opposed to the mean bubble size of 6.2 mm estimated by the correlation of Geary and Rice [70]. As it is possible to see from Fig. 10, the agreement with the experiment in terms of pH prediction improves, even tough the mass transfer rates in the first part of the reaction experiment is faster as depicted in Fig. 11 and the changes in terms of the time-averaged mean Sauter diameter at different heights of the column shown in Fig. 13 are not so remarked. It is worth reminding that the mass transfer rates depend on the local bubble size distribution, therefore the comparison in terms of the sole mean Sauter diameter may be limiting, as this can be very different in the two investigated cases. Also the comparison in terms of global gas holdup and plume oscillating period reported in Table 3 shows an improvement in the prediction, while negligible differences are detected in the time-averaged axial gas velocity profiles of Fig. 12. The comparison between these two cases clearly pointed out the need of reliable boundary conditions for similar simulations [35], which is an aspect often overlooked when similar test cases are considered both on the experimental and modeling point of view. However, even without any knowledge of the mean bubble size formed by the gas sparger, the results obtained by means of the use of standard correlations are in general satisfactory, also in the reactive case considered in this work.

## 5. Conclusions

In this work our own QMOM implementation in the OpenFOAM (v. 2.2.x) solver `compressibleTwoPhaseEulerFoam` has been used to simulate, for the first time, a reacting gas–liquid system. Simulation results, obtained with a fully predictive model with no adjustable modeling parameters, are compared with experiments, resulting in a good agreement. The model seems to be able to correctly predict the fluid dynamics of the bubble column, the evolution of the bubble size and the mass transfer rate between gas and liquid. This methodology was proven to offer a great advantage over modeling approaches without population balance, since the bubble size becomes a fitting parameter, rather than a purely dynamic variable influencing mass transfer rates as in the physical reality. Although the methodology contains numerous sub-models taking care of different portion of the physics, the overall results are good when the comparison with experimental data is performed, especially in terms of the pH time evolution which is the easiest and most reliable experimental measurement carried out in this case. The agreement in terms of pH is an indirect sign that also bubble size and other fluid dynamic quantities are in decent agreement with the experimental reality (considering also the experimental uncertainty). Future steps of this work include the extension of this methodology to the simulation of liquid–liquid dispersions, the development of reliable methodologies for dealing with poly-celerity (i.e. bubble gas velocity dependent on bubble size resulting in different moment velocities) and the development of more reliable kernels for coalescence and breakage.

## References

[1] D.L. Marchisio, R.O. Fox, Computational Models for Polydisperse Particulate and Multiphase Systems, Cambridge University Press, Cambridge, UK, 2013.
[2] V.V. Ranade, Computational Flow Modeling for Chemical Reactor Engineering, Academic Press, San Diego, USA, 2002.
[3] I. Roghair, M. Baltussen, M.V.S. Annaland, J. Kuipers, Direct numerical simulations of the drag force of bi-disperse bubble swarms, Chem. Eng. Sci. 95 (2013) 48–53.

[4] V.V. Buwa, D.S. Deo, V.V. Ranade, Eulerian–Lagrangian simulations of unsteady gas–liquid flows in bubble columns, Int. J. Multiph. Flow 32 (2006) 864–885.
[5] A. Couzinet, B. Bédat, O. Simonin, Numerical study and Lagrangian modelling of turbulent heat transport, Flow Turbul. Combust. 80 (2008) 37–46.
[6] D. Pfleger, S. Gomes, N. Gilbert, H.G. Wagner, Hydrodynamic simulations of laboratory scale bubble columns fundamental studies of the Eulerian–Eulerian modelling approach, Chem. Eng. Sci. 54 (1999) 5091–5099.
[7] D. Pfleger, S. Becker, Modelling and simulation of the dynamic flow behaviour in a bubble column, Chem. Eng. Sci. 56 (2001) 1737–1747.
[8] R.F. Mudde, O. Simonin, Two- and three-dimensional simulations of a bubble plume using a two-fluid model, Chem. Eng. Sci. 54 (1999) 5061–5069.
[9] G. Montante, A. Paglianti, F. Magelli, Experimental analysis and computational modelling of gas–liquid stirred vessels, Chem. Eng. Res. Des. 85 (2007) 647–653.
[10] R.S. Oey, R.F. Mudde, H.E.A. Van Den Akker, Sensitivity study on interfacial closure laws in two-fluid bubbly flow simulations, AIChE J. 49 (2003) 1621–1636.
[11] V.V. Buwa, V.V. Ranade, Dynamics of gas–liquid flow in a rectangular bubble column: experiments and single/multi-group CFD simulations, Chem. Eng. Sci. 57 (2002) 4715–4736.
[12] S. Cheung, G. Yeoh, J. Tu, On the numerical study of isothermal vertical bubbly flow using two population balance approaches, Chem. Eng. Sci. 62 (2007) 4659–4674.
[13] S. Cheung, G. Yeoh, J. Tu, Population balance modeling of bubbly flows considering the hydrodynamics and thermomechanical processes, AIChE J. 54 (7) (2008) 1689–1710.
[14] E. Krepper, D. Lucas, T. Frank, H.M. Prasser, P.J. Zwart, The inhomogeneous musig model for the simulation of polydispersed flows, Nucl. Eng. Des. 238 (2008) 1690–1702.
[15] M.R. Bhole, J.B. Joshi, D. Ramkrishna, Cfd simulation of bubble columns incorporating population balance modeling, Chem. Eng. Sci. 63 (2008) 2267–2282.
[16] S. Cheung, G. Yeoh, J. Tu, A review of population balance modelling for isothermal bubbly flows, J. Comput. Multiph. Flows 1 (2009) 161–199.
[17] X.Y. Duan, S.C.P. Cheung, G.H. Yeoh, J.Y. Tu, E. Krepper, D. Lucas, Gas–liquid flows in medium and large vertical pipes, Chem. Eng. Sci. 66 (2011) 872–883.
[18] Y. Liao, R. Rzehak, D. Lucas, E. Krepper, Baseline closure model for dispersed bubbly flow: bubble coalescence and breakup, Chem. Eng. Sci. 122 (2015) 336–349.
[19] M. Petitti, A. Nasuti, D.L. Marchisio, M. Vanni, G. Baldi, N. Mancini, F. Podenzani, Bubble size distribution modeling in stirred gas–liquid reactors with QMOM augmented by a new correction algorithm, AIChE J. 56 (2010) 36–53.
[20] A. Buffo, M. Vanni, D.L. Marchisio, Multidimensional population balance model for the simulation of turbulent gas–liquid systems in stirred tank reactors, Chem. Eng. Sci. 70 (2012) 31–44.
[21] A. Buffo, M. Vanni, D.L. Marchisio, R.O. Fox, Multivariate quadrature-based moments methods for turbulent polydisperse gas–liquid systems, Int. J. Multiph. Flow 50 (2013) 41–57.
[22] A. Buffo, D.L. Marchisio, Modeling and simulation of turbulent polydisperse gas–liquid systems via the generalized population balance equation, Rev. Chem. Eng. 30 (2014) 73–126.
[23] T. Acher, P. Dems, S. Lenz, C. Gobert, W. Polifke, A quadrature method of moments for polydisperse flow in bubble columns including poly-celerity, breakup and coalescence, J. Comput. Multiph. Flows 6 (2014) 457–474.
[24] T. Acher, A Moments Model for the Numerical Simulation of Bubble Column Flows, Technische Universität München, Munich, Germany, 2015 Ph.D. thesis.
[25] A. Buffo, M. Vanni, P. Renze, D. Marchisio, Empirical drag closure for polydisperse gas liquid systems in bubbly flow regime: bubble swarm and micro-scale turbulence, Chem. Eng. Res. Des. 113 (2016) 284–303.
[26] D. Ramkrishna, Population Balances: Theory and Applications to Particulate Systems in Engineering, 1st ed., Academic Press, San Diego, USA, 2000.
[27] G.H. Yeoh, J. Tu, Computational Techniques for Multiphase Flows, Butterworth-Heinemann, Oxford, UK, 2010.
[28] J. Sanyal, D.L. Marchisio, R.O. Fox, K. Dhanasekharan, On the comparison between population balance models for cfd simulation of bubble columns, Ind. Eng. Chem. Res. 44 (2005) 5063–5072.
[29] B. Selma, R. Bannari, P. Proulx, Simulation of bubbly flows: comparison between direct quadrature method of moments (DQMOM) and method of classes (CM), Chem. Eng. Sci. 65 (2010) 1925–1941.
[30] H.M. Hulburt, S. Katz, Some problems in particle technology: a statistical mechanical formulation, Chem. Eng. Sci. 19 (1964) 555–574.
[31] R. McGraw, Description of aerosol dynamics by the quadrature method of moments, Aerosol Sci. Technol. 27 (1997) 255–265.
[32] R.G. Gordon, Error bounds in equilibrium statistical mechanics, J. Math. Phys. 9 (1968) 655–663.
[33] J.C. Wheeler, Modified moments and gaussian quadratures, Rocky Mt. J. Math. 4 (1974) 287–296.
[34] W. Gautschi, Orthogonal Polynomials: Computation and Approximation, Oxford University Press, Oxford, UK, 2004.
[35] A. Buffo, D.L. Marchisio, M. Vanni, P. Renze, Simulation of polydisperse multiphase systems using population balances and example application to bubbly flows, Chem. Eng. Res. Des. 91 (2013) 1859–1875.
[36] M. Icardi, G. Ronco, D.L. Marchisio, M. Labois, Efficient simulation of gas–liquid pipe flows using a generalized population balance equation coupled with the algebraic slip model, Appl. Math. Model. 38 (2014) 4277–4290.
[37] M. Petitti, M. Vanni, D.L. Marchisio, A. Buffo, F. Podenzani, Simulation of coalescence, break-up and mass transfer in a gas–liquid stirred tank with CQMOM, Chem. Eng. J. 228 (2013) 1182–1194.
[38] P. Renze, A. Buffo, D. Marchisio, M. Vanni, Simulation of coalescence, breakup, and mass transfer in polydisperse multiphase flows, Chem. Ing. Tech. 86 (2014) 1088–1098.
[39] V. Vikas, C. Yuan, Z.J. Wang, R.O. Fox, Modeling of bubble-column flows with quadrature-based moment methods, Chem. Eng. Sci. 66 (2011) 3058–3070.
[40] D. Darmana, R. Henket, N. Deen, J. Kuipers, Detailed modelling of hydrodynamics, mass transfer and chemical reactions in a bubble column using a discrete bubble model: chemisorption of $CO_2$ into NaOH solution, numerical and experimental study, Chem. Eng. Sci. 62 (2007) 2556–2575.
[41] D. Lucas, E. Krepper, H.M. Prasser, Use of models for lift, wall and turbulent dispersion forces acting on bubbles for poly-disperse flows, Chem. Eng. Sci. 62 (2007) 4146–4157.
[42] D. Lucas, A. Tomiyama, On the role of the lateral lift force in poly-dispersed bubbly flows, Int. J. Multiph. Flow 37 (9) (2011) 1178–1190.
[43] I. Roghair, Y. Lau, N. Deen, H. Slagter, M. Baltussen, M. Van Sint Annaland, J. Kuipers, On the drag force of bubbles in bubble swarms at intermediate and high Reynolds numbers, Chem. Eng. Sci. 66 (2011) 3204–3211.
[44] C.Y. Wen, Y.H. Yu, Mechanics of fluidization, Chem. Eng. Prog. Symp. Ser. 62 (1966) 100–111.
[45] A. Bakker, H.E.A. Van den Akker, Gas–liquid contacting with axial flow impellers, Chem. Eng. Res. Des. 72 (1994) 573–582.
[46] D. Colombet, D. Legendre, F. Risso, A. Cockx, P. Guiraud, Dynamics and mass transfer of rising bubbles in a homogenous swarm at large gas volume fraction, J. Fluid Mech. 763 (2015) 254–285.
[47] D.L. Marchisio, R.D. Vigil, R.O. Fox, Implementation of the quadrature method of moments in CFD codes for aggregation-breakage problems, Chem. Eng. Sci. 58 (2003a) 3337–3351.
[48] D.L. Marchisio, R.D. Vigil, R.O. Fox, Quadrature method of moments for aggregation-breakage processes, J. Colloid Interface Sci. 258 (2003b) 322–334.
[49] Y. Liao, D. Lucas, A literature review on mechanisms and models for the coalescence process of fluid particles, Chem. Eng. Sci. 65 (2010) 2851–2864.
[50] Y. Liao, D. Lucas, A literature review of theoretical models for drop and bubble breakup in turbulent dispersions, Chem. Eng. Sci. 64 (2009) 3389–3406.
[51] M. Laakkonen, V. Alopaeus, J. Aittamaa, Validation of bubble breakage, coalescence and mass transfer models for gas–liquid dispersion in agitated vessel, Chem. Eng. Sci. 61 (2006) 218–228.
[52] M. Laakkonen, P. Moilanen, V. Alopaeus, J. Aittamaa, Modelling local bubble size distributions in agitated vessels, Chem. Eng. Sci. 62 (2007) 721–740.

[53] V. Alopaeus, J. Koskinen, K. Keskinen, J. Majander, Simulation of the population balances for liquid-liquid systems in a nonideal stirred tank. Part 2-parameter fitting and the use of the multiblock model for dense dispersions, Chem. Eng. Sci. 57 (2002) 1815–1825.
[54] J.C. Lamont, D.S. Scott, An eddy cell model of mass transfer into the surface of a turbulent liquid, AIChE J. 16 (1970) 513–519.
[55] R. Pohorecki, W. Moniuk, Kinetics of reaction between carbon dioxide and hydroxyl ions in aqueous electrolytic solutions, Chem. Eng. Sci. 43 (1988) 1677–1684.
[56] T.J. Edwards, G. Maurer, J. Newman, J.M. Prausnitz, Vapor–liquid equilibria in multicomponent aqueous solutions of volatile weak electrolytes, AIChE J. 24 (1978) 966–976.
[57] C. Tsonopolous, D.M. Coulson, L.W. Inman, Ionization constants of water pollutants, J. Chem. Eng. Data 21 (1976) 190–193.
[58] M. Eigen, Method for investigation of ionic reactions in aqueous solutions with half times as short as $10^{-9}$ s, Discuss. Faraday Soc. 17 (1954) 194–205.
[59] H. Hikita, S. Asai, T. Takatsuka, Absorption of carbon dioxide into aqueous sodium hydroxide and sodium carbonate–bicarbonate solutions, Chem. Eng. J. 11 (1976) 131–141.
[60] S. Weisenberger, A. Schumpe, Estimation of gas solubility in salt solutions at temperatures from 273 to 363 K, AIChE J. 42 (1996) 298–300.
[61] G.F. Versteeg, W.P.M. van Swaaij, Solubility and diffusivity of acid gases ($CO_2$ and $N_2O$) in aqueous alkaloamine solutions, Journal of Chemical Engineering Data 33 (1988) 29–34.
[62] G.A. Ratcliff, J.G. Holdcroft, Diffusivities of gases in aqueous electrolyte solutions, Trans. Inst. Chem. Eng. Chem. Eng. 41 (1963) 315–319.
[63] K.R. Westerterp, W.P.M. van Swaaij, A.A.C.M. Beenackers, Chemical Reactor Design and Operation, Wiley, New York, USA, 1984.
[64] A. Buffo, M. Vanni, D. Marchisio, On the implementation of moment transport equations in openfoam: Boundedness and realizability, Int. J. Multiph. Flow 85 (2016) 223–235.
[65] J.H. Ferziger, M. Peric, Computational Methods for Fluid Dynamics, 3rd edition, Springer, Berlin, Germany, 2001.
[66] H.F. Trotter, On the product of semi-groups of operators, Proc. Amer. Math. Soc., 10 (1959) 545–551.
[67] G. Strang, On the construction and comparison of difference schemes, SIAM J. Numer. Anal. 5 (1968) 506–517.
[68] H. Holden, K.H. Karlsen, K.-A. Lie, N.H. Risebro, Splitting Methods for Partial Differential Equations with Rough Solutions, European Mathematical Society Publishing House, Zurich, Switzerland, 2010.
[69] A.C. Hindmarsh, ODEPACK: a systematized collection of ODE solvers, in: R.S. Stepleman (Ed.), Scientific Computing, North-Holland, Amsterdam, Netherlands, 1983, pp. 55–64.
[70] N.W. Geary, R.G. Rice, Bubble size prediction for rigid and flexible spargers, AIChE J. 37 (1991) 161–168.
[71] R. Clift, J.R. Grace, M.E. Weber, Bubbles, Drops, and Particles, Dover Publications, New York, USA, 1978.